

Suzaku Observation of the Anomalous X-ray Pulsar 1E 1841–045

Mikio MORII^{1,2}, Shunji KITAMOTO², Noriaki SHIBAZAKI², Nobuyuki KAWAI¹,
Makoto ARIMOTO¹, Masaru UENO¹, Takayoshi KOHMURA³, Yukikatsu TERADA⁴,
Shigeo YAMAUCHI⁵, and Hiromitsu TAKAHASHI⁶

¹*Department of Physics, Tokyo Institute of Technology, Ookayama 2-12-1, Meguro-ku,
Tokyo 152-8551, Japan*

morii.m.ab@m.titech.ac.jp, mmorii@rikkyo.ac.jp

²*Department of Physics, Rikkyo University, Nishi-ikebukuro 3-34-1, Toshima-ku, Tokyo 171-8501, Japan*

³*Physics Department, Kogakuin University 2665-1 Nakano-cho, Hachioji, Tokyo 192-0015, Japan*

⁴*Cosmic Radiation Laboratory, Institute of Physical and Chemical Research, Wako, Saitama 351-0198, Japan*

⁵*Department of Physics, Faculty of Science, Nara Women's University Kita-uoyanishi-machi,
Nara 630-8506, Japan*

⁶*Department of Physical Science, School of Science, Hiroshima University 1-3-1 Kagamiyama,
Higashi-Hiroshima, Hiroshima 739-8526, Japan*

(Received 2010 July 7; accepted 2010 July 7)

Abstract

We report the results of a Suzaku observation of the anomalous X-ray pulsar (AXP) 1E 1841–045 at a center of the supernova remnant Kes 73. We confirmed that the energy-dependent spectral models obtained by the previous separate observations were also satisfied over a wide energy range from 0.4 to ~ 70 keV, simultaneously. Here, the models below ~ 10 keV were a combination of blackbody (BB) and power-law (PL) functions or of two BBs with different temperatures at 0.6 – 7.0 keV (Morii et al. 2003), and that above ~ 20 keV was a PL function (Kuiper, Hermsen, & Mendez 2004). The combination BB + PL + PL was found to best represent the phase-averaged spectrum. Phase-resolved spectroscopy indicated the existence of two emission regions, one with a thermal and the other with a non-thermal nature. The combination BB + BB + PL was also found to represent the phase-averaged spectrum well. However, we found that this model is physically unacceptable due to an excessively large area of the emission region of the blackbody. Nonetheless, we found that the temperatures and radii of the two blackbody components showed moderate correlations in the phase-resolved spectra. The fact that the same correlations have been observed between the phase-averaged spectra of various magnetars (Nakagawa et al. 2009) suggests that a self-similar function can approximate the intrinsic energy

spectra of magnetars below ~ 10 keV.

Key words: stars: neutron — stars: pulsars: individual (1E 1841–045) — X-rays: individual (1E 1841–045, Kes 73)

1. Introduction

Anomalous X-ray pulsars (AXPs) are thought to be magnetars, which are strongly magnetized neutron stars with emissions powered by dissipation of magnetic energy (see Woods & Thompson (2006) for a recent review). So far, about 10 AXPs have been reported as well-confirmed objects or candidates. They are distributed along the Galactic plane and within the Small Magellanic Cloud. They are characterized as follows: (1) The spin periods (P) are concentrated within the narrow range of 2 – 12 s. In addition, their spin-down rates (\dot{P}) are large ($5 \times 10^{-13} - 1 \times 10^{-10} \text{ s s}^{-1}$). Both of these facts imply that they have strong dipole magnetic fields of $10^{14} - 10^{15}$ G at their surfaces. (2) Their X-ray luminosities ($L_X \sim 10^{34} - 10^{36} \text{ ergs s}^{-1}$) exceed the rate of spin-down energy loss of neutron stars ($\dot{E} = 4\pi^2 I \dot{P} / P^3 \sim 10^{32.6} \text{ ergs s}^{-1}$, where $I \simeq 10^{45} \text{ g cm}^2$ is the momentum of inertia of a neutron star.). This fact suggests that AXPs are not rotation-powered pulsars. (3) Timing characteristics peculiar to accretion-powered pulsars, such as a large amount of timing noise and persistent spin-up periods have not been observed to date. (4) Whereas persistent radio emissions have not been detected, transient pulsed radio emissions were found for transient AXPs, XTE J1810–197 (Camilo et al. 2006) and 1E 1547.0–5408 (Camilo et al. 2007). (5) Some AXPs produced spiky short bursts with durations $\Delta t \sim 0.1$ s, similar to those observed in soft gamma repeaters (SGRs), which are also magnetar candidates. (6) They have peculiar energy spectra which will be described below.

Energy spectra of AXPs below ~ 10 keV can empirically be modeled well by either a combination of a blackbody and a power-law function or two blackbody functions. Fitting the spectra using the former model yields a blackbody temperatures of about 0.4 keV and the photon indices are within the range of 2.0 – 4.6 (Woods & Thompson 2006). Recently, using the latter model, Nakagawa et al. (2009) reported that there are correlations between the temperatures and radii of the two blackbodies. On the other hand, non-thermal, hard X-ray emissions with large pulse fractions were discovered from some AXPs above ~ 10 keV (Kuiper et al. 2006). Their total and pulsed spectra were found to have power-law shapes. The photon indices of the total spectra were in a range from 1.0 to 1.4, and those of the pulsed spectra in a range from -1.0 to 1.0. These emissions were detected up to ~ 220 keV (Kuiper et al. 2006; den Hartog et al. 2008; den Hartog, Kuiper & Hermsen 2008). Some theoretical models of the hard X-ray emission were proposed, based on thermal bremsstrahlung (Thompson & Beloborodov 2005; Beloborodov & Thompson 2007), synchrotron radiation (Thompson & Beloborodov 2005; Beloborodov & Thompson 2007), and emission caused by QED (quantum

electrodynamics) effects (Heyl & Hernquist 2005). However, the emission mechanism is still not clearly understood.

One AXP candidate is 1E 1841–045 (Hellier 1994; Mereghetti & Stella 1995; van Paradijs, Taam & van den Heuvel 1995). It is located at the center of the supernova remnant (SNR) Kes 73 (G 27.4+0.0; Kriss et al. 1985) with a diameter of about 4' (Morii et al. 2003). The kinematic distance to the SNR was originally estimated to be between 6 and 7.5 kpc (Sanbonmatsu & Helfand 1992). Recently, this distance was revised to be between 7.5 and ~ 9.8 kpc by Tian & Leahy (2007). The pulse period of 1E 1841–045 was determined to be 11.8 s (Vasisht & Gotthelf 1997). Its activity has been continuously monitored by the Rossi X-ray Timing Explorer (RXTE) (Dib, Kaspi & Gavriil 2008), and although several glitches occurred during the monitoring period, there is no evidence for any pulsed flux change in the 2–10 keV band. Using Chandra data in the 0.6 – 7.0 keV region, Morii et al. (2003) reported that the spectrum could be modeled well using a model consisting of a blackbody ($kT = 0.44 \pm 0.02$ keV) and a power-law function with the hardest photon index yet measured for AXPs ($\Gamma = 2.0 \pm 0.3$). In their analysis, they showed that the two-blackbody model ($kT = 0.47 \pm 0.02$ keV and $kT = 1.5_{-0.1}^{+0.2}$ keV) also fitted well. In addition, they showed that there were two emission regions and the emissions appeared as two peaks in the pulse profile. The peaks were interpreted as blackbody emission from a hot spot and non-thermal emission from another region, although blackbody emissions from two hot spots were also a possible explanation. Kuiper, Hermsen, & Mendez (2004) discovered the very hard (photon index: 0.94 ± 0.16) pulsed X-ray emission up to ~ 150 keV, using the RXTE Proportional Counter Array (PCA; 1.8 – 23.8 keV) and the High Energy X-ray Timing Experiment (HEXTE; 15 – 250 keV). The discovery of the hard X-ray component compels a reconsideration of the spectral models below ~ 10 keV, because this component is thought to account for a substantial fraction in an energy range below ~ 10 keV.

In this paper, we report on results obtained from a Suzaku observation of AXP 1E 1841–045. Thanks to the wide energy coverage of Suzaku, we obtained a continuous spectrum from 0.4 to ~ 70 keV. Spectroscopic data over such a wide energy band offers advantages in decomposing a spectrum into its constituent components.

2. Observation

1E 1841–045 and Kes 73 were observed by the fifth Japanese X-ray satellite Suzaku on April 19–22, 2006, as a target of AO-1. Suzaku (Mitsuda et al. 2007) has two types of X-ray detectors in operation: the X-ray Imaging Spectrometer (XIS; Koyama et al. 2007) and the Hard X-ray Detector (HXD; Takahashi et al. 2007; Kokubun et al. 2007). Four XISs are mounted at the foci of four X-ray telescopes (XRT; Serlemitsos et al. 2007) with a moderate angular resolution of 2 (half power diameter; HPD). Three of the XISs (XIS0, XIS2, and XIS3) are front-illuminated (FI) CCDs, sensitive in the energy range of 0.4–12 keV, and the remaining one (XIS1) is a back-illuminated (BI) CCD, sensitive in the energy range of 0.2–12 keV. We

chose the “1/8 window mode” of the XISs to obtain a time resolution of 1 s, which corresponds to 0.08 times the pulsation period of this AXP. This mode covered a field of view (FoV) of $17'8'' \times 2'2''$ (1024×128 pixels).

The HXD is a non-imaging, collimated hard X-ray detector sensitive in the energy range of 10–600 keV. It is composed of PIN photodiodes and GSO scintillators mounted in a well of collimator shields, which cover the energy regions 10–70 keV and 50–600 keV, with a field of view of $34' \times 34'$ ($\lesssim 100$ keV) and $4'5'' \times 4'5''$ ($\gtrsim 100$ keV), respectively. The time resolution during our observations was 61 μ s.

Our observations were carried out at the position (RA, Dec) = ($18^{\text{h}}41^{\text{m}}15^{\text{s}}.5$, $-4^{\circ}51'24''.5$) (J2000.0) at the HXD nominal pointing.

3. Analysis

We followed the procedure outlined in the “seven steps” manuals for XIS and HXD analyses^{1,2}. We used the cleaned events generated by the standard pipeline processing of rev-1.2.

For the XIS analysis, we removed the timeslice 13:05 – 14:42 (UTC) on April 20, 2006, because a temperature anomaly of XIS2 was reported³. We selected as source and background regions a concentric circle and annulus whose central positions were at the peak position of the AXP. The radius of the source circle was set to $4'33''$, and the radii of the inner and outer boundaries of the background annulus were set to $4'33''$ and $6'00''$, respectively. We then set the source and background regions as the intersections of these concentric regions and the 1/8 window regions of the XISs. The net exposure times for the XISs were 95.3 ks.

For the PIN and GSO analyses we used a background file made by the LCFIT (bgd_d) method of version 1.2 v.0611. This observation was performed in the period from March 14 to May 13, 2006, when the HXD was operated with a lower discriminator level for the PSD cut. This caused an increase in the GSO events and saturation of the internal data transfer sometimes occurred, especially during periods of high count rates due to background particles. Since the uncertainty in the source flux was higher during these periods, we applied an additional GTI (good time interval) to remove these periods according to the recommendations of the detector team⁴ in addition to the normal GTI made by the event and background files. The net exposures for the PIN and GSO were 57.8 ks.

We checked the light curves of all XISs and the PIN binned at 300, 10 and 1 s, and found no notable variation due to background changes, instrument trouble or AXP activity.

¹ http://www.astro.isas.jaxa.jp/suzaku/analysis/7step_XIS_20061218.txt

² http://www.astro.isas.jaxa.jp/suzaku/analysis/7step_HXD_20070305.txt

³ <http://www.astro.isas.jaxa.jp/suzaku/log/xis/>

⁴ <http://www.astro.isas.jaxa.jp/suzaku/analysis/hxd/hxdgti/>

4. Timing Analysis

It is known that the time tagged for each XIS frame in the 1/8 window mode was 7 s earlier than that of the HXD ⁵, whereas the time tagging of the HXD is well calibrated by comparison with other satellites, such as RXTE, INTEGRAL, and Swift (Terada et al. 2008). We corrected the XIS frame times by adding 7 s to the reference time "MJDREFF". We corrected photon arrival times into those at the solar barycenter by using `aebarycen` (ver. 2006-08-02). We constructed the overall light curve by summing the light curves of all the XISs for the source region with 1 s binning in an energy range of 0.4 – 10.0 keV. We searched for periodicity in this light curve using `xronos/powspec` and determined the pulse period more precisely using `xronos/efsearch`. The pulse period obtained in this manner was 11.7830 ± 0.0002 s at the epoch of 53845.7951888 (MJD), which is consistent with the phase coherent ephemeris obtained by Dib, Kaspi & Gavriil (2008). We also searched for periodicity in the PIN light curve in the energy range of 12.0 – 50.0 keV using the Z_1^2 method (Buccheri et al. 1983). We detected the signal significantly in the null hypothesis probability of 1.2×10^{-5} . For the GSO light curves (40 – 60, 50 – 100 and 100 – 600 keV) we could not find a signal corresponding to the pulse period of the AXP.

We made pulse profiles for three energy ranges (0.6 – 3.0, 3.0 – 10.0 and 12.0 – 30.0 keV) by folding the light curves with the pulse period obtained at the same epoch (figure 1). Here, for the XIS light curves (0.6 – 3.0 and 3.0 – 10.0 keV), non-X-ray and X-ray backgrounds were subtracted by selecting the background region as described in section 3. For the PIN light curve (12.0 – 30.0 keV) only the non-X-ray background ($0.337 \pm 0.010(\text{syst})$ counts s^{-1} with a systematic uncertainty of 3%. ⁶) was subtracted and the X-ray background was retained. The pulse fraction (PF), defined as $PF = [\sum(R_i - R_{\min})] / \sum R_i$, for these bands was $6.6 \pm 0.7(\text{stat})\%$, $17.2 \pm 1.1(\text{stat})\%$ and $32.9 \pm 7.0(\text{stat}) \pm 8.9(\text{syst})\%$, respectively. Here, R_i and R_{\min} denote the count rate in the i -th phase bin and the minimum count rate among all the phase bins, respectively. The errors denoted by "(stat)" and "(syst)" represent a statistical error of 1σ , and a systematic error due to the 3% uncertainty in the non-X-ray background of the PIN ⁶. We will use this convention from this point onwards. In the PIN energy range (12.0 – 30.0 keV) the pulsed fraction increased to $60.8 \pm 13.1(\text{stat}) \pm 16.8(\text{syst})\%$ after subtracting both the non-X-ray and X-ray backgrounds. Here, we estimated the count rate for the X-ray background to be 0.0489 counts s^{-1} (subsection 5.2). Although this is larger than the value of $\sim 25\%$ at 20 keV reported by Kuiper et al. (2006), the difference is not significant due to the large uncertainty in the pulsed fraction for the PIN.

We also made plots of the hardness ratios of the second pulse profile to the first, and of the third to the second. To eliminate the constant component the count rate at the pulse

⁵ <http://www.astro.isas.ac.jp/suzaku/analysis/xis/timing/>

⁶ Suzaku-memo 2006-42, 2006-43: <http://www.astro.isas.jaxa.jp/suzaku/doc/suzakumemo/>

minimum phase (0.0 – 0.125) was subtracted before the division. It can be seen that the spectrum at the second peak of the pulse profile was harder than that of the first, which is consistent with the result obtained by the previous Chandra observation (e.g. Morii et al. 2003).

5. Energy Spectrum

5.1. Spectroscopy of the SNR Kes 73 using the Chandra Data

Due to the point spread function (PSF) of the XRTs (HPD = 2') the spectrum of the AXP was contaminated by the surrounding SNR Kes 73. Therefore, we must determine the spectral model of the SNR before performing spectral analyses with the Suzaku data. For this purpose, we analyzed archival data of the Chandra observation taken with the AXAF CCD Imaging Spectrometer (ACIS) in the TE mode (Observation ID: 729). We extracted the pure SNR spectrum by spatially excluding the AXP and the charge trailing regions. We then attempted to fit the entire SNR spectrum using the `vnei`, `vpshock`, and `vsedov` models (Borkowski et al. 2001). It was found that the entire SNR spectrum could be modeled by the `vsedov` model (see figure 2). Although even the best model was statistically unacceptable, globally, the fit appeared good and residuals were present only at the emission lines. Therefore, we believe that such local residuals in the SNR model would not affect the interpretation of the Suzaku spectroscopic data for the AXP spectrum, because the AXP spectrum is composed only of continuum components.

Moreover, the spreading due to the wide angular response of the XRTs would effectively homogenize spatial variation in the SNR spectrum. Therefore, we can assume that the spectrum of the SNR is spatially uniform. Consequently, in the following section we will use the SNR spectral model obtained here as the SNR component. Further analysis was carried out on the SNR data, but the details are beyond the scope of this paper, and will be published at a later date.

5.2. Preparation of the Suzaku Data: Estimation of Backgrounds and Calibrations

We analyzed the XISs and PIN source spectra after subtracting the corresponding backgrounds. Here, the source and background spectra of XISs were extracted from the regions shown in section 3 and the non-X-ray background was subtracted in the case of the PINs. We made the response files (RMF; Redistribution Matrix File and ARF; Ancillary Response File) of the XISs by using `xisrmfgen` and `xissimarfgen`. For the response of the PIN, we used that for a point source at the nominal position of the HXD (`ae_hxd_pinhxnom_20060814.rsp`). For the spectral fits we used `xspec11` in `HEADAS v6.3.2`. We rebinned the PI spectra of the XISs so that at least N_{\min} counts could be contained in each bin by using `grppha`. Here, we set the counts N_{\min} to 50, 100, 500, 100, and 50 for energy intervals of less than 0.9, 0.9 – 1.2, 1.2 – 3.0, 3.0 – 5.0, and more than 5.0 keV, respectively. We used $N_{\min} = 800$ counts for the PIN

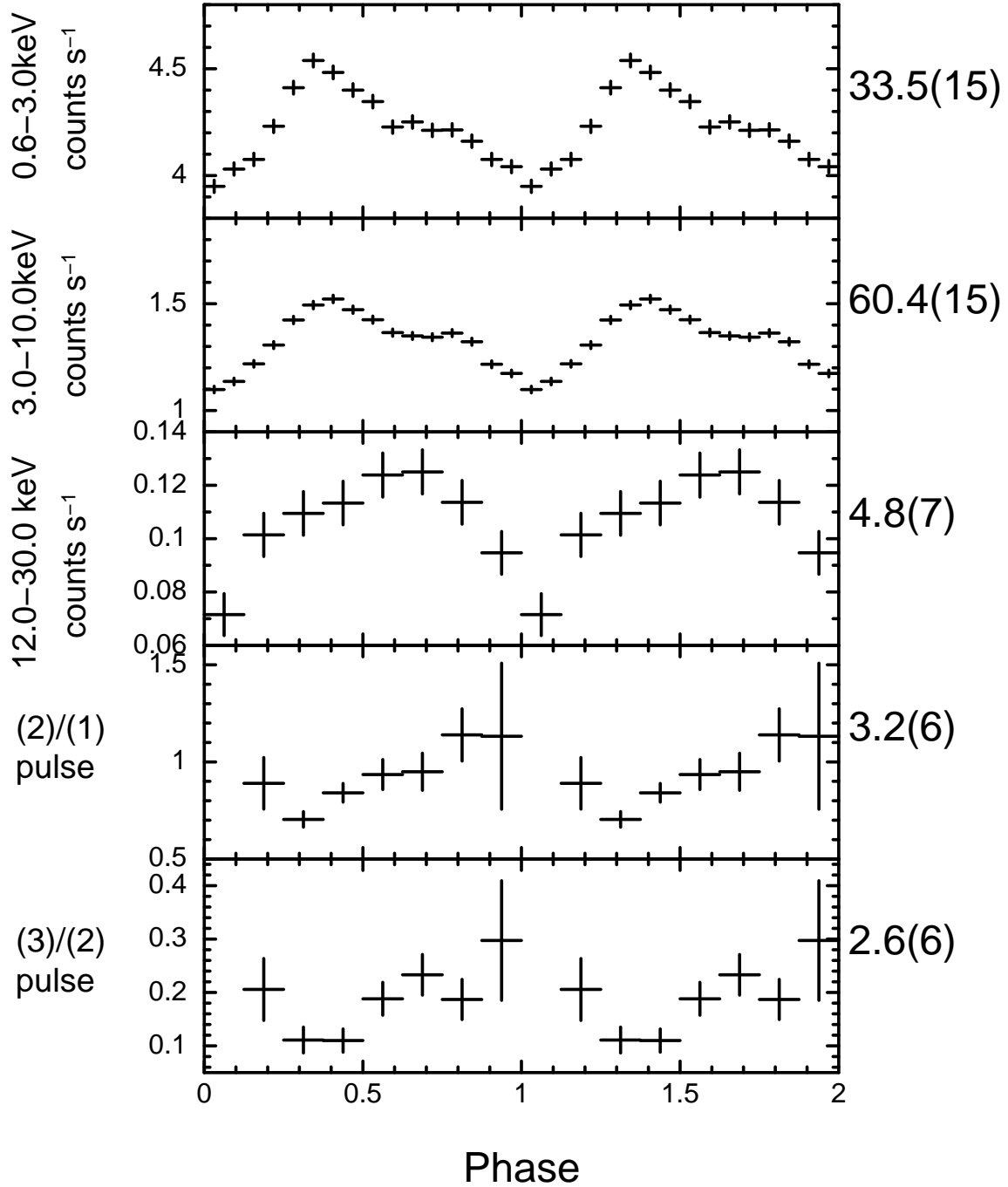


Fig. 1. Folded pulse profiles and hardness ratios. The top two panels show pulse profiles made by the sum of all XISs in the energy ranges of 0.6 – 3.0 keV and 3.0 – 10.0 keV. The third panel shows a pulse profile for the PIN in an energy range of 12 – 30 keV. The vertical axes have units of count rate (counts s⁻¹) after the corresponding background-subtractions (section 4). The fourth and fifth panels show the hardness ratios of the pulsed component, which are the ratios of the photon count rates in the second to the first panel and the third to the second, respectively, after subtracting the photon count rates at the pulse minimum phases (phase = 0.0 – 0.125). The horizontal axes show the pulse phase up to 2 periods. The vertical error bars in all panels represent 1 σ levels. At the right of each panel the reduced χ^2 and the degree of freedom are shown for the case of fitting the profile to a constant model.

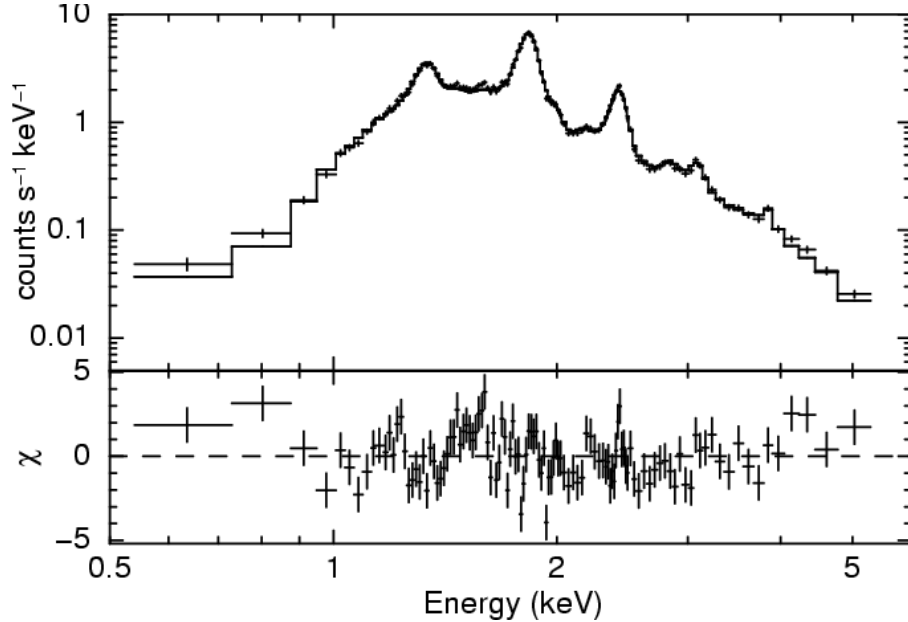


Fig. 2. Spectrum of Kes 73 taken by Chandra, fitted by the `vsedov` model with the optimum parameters. The vertical bars represent 1σ errors.

spectrum. We followed the next steps for the spectral fitting.

(1) To fix the gain uncertainty of the XISs we fitted only the XISs data by a model, $c_{\text{det}} \times (c_{\text{SNR}} \times \text{SNR} + \text{AXP})$, while the gain parameters (energy scales and offsets) were allowed to vary. Here, SNR and AXP are self-explanatory spectral components. The parameter c_{SNR} denotes the normalization of the SNR component. It was used to compensate for the discrepancy in the SNR flux between this observation and the Chandra observation, which was caused by the small coverage area of the SNR region in the 1/8 window mode of the XISs. The parameters c_{det} ($\text{det} = \text{XIS0}, \text{XIS1}, \text{XIS2}, \text{and XIS3}$) represent normalizations of the detectors. They were used to compensate for the relative flux uncertainty among the XISs, fixing c_{XIS0} to be 1. This flux uncertainty was caused by the systematic uncertainty of the ARF generated by `xissimarfgen`, which has a systematic uncertainty for small regions such as those used in this analysis (section 3).

(2) Fixing the gain parameters determined using the first step, we fitted the XISs and PIN data simultaneously using a model, $c_{\text{det}} \times (c_{\text{SNR}} \times \text{SNR} + \text{AXP} + \text{CXB} + \text{GRXE})$. Here, CXB and GRXE denote the spectral components from the cosmic X-ray background and the Galactic ridge X-ray emission. The CXB + GRXE component was taken into consideration only for the HXD/PIN, because in the case of the XISs this component could be removed by the background subtraction shown in section 3.

The CXB + GRXE component was estimated by using additional Suzaku data from the GRXE observation at the field ($l = 28^\circ.5, b = -0^\circ.2$). Fortunately, this field is very close to the pointing field of the AXP, ($l = 27^\circ.5, b = 0^\circ.0$), so this estimation is expected to produce a

reasonable result. The spectrum of the PIN at ($l = 28^\circ.5$, $b = -0^\circ.2$) was fitted by a power-law function (“pegpwlw” model) using the response file for a point source at the nominal position of the HXD (ae_hxd_pinhxnom_20060814_w23.rsp). This fitting resulted in a normalization of $17.5_{-1.8}^{+2.0}$ (stat) $\times 10^{-12}$ erg/cm²/s in the energy range 10 – 50 keV and a photon index of $2.64_{-0.39}^{+0.43}$ (stat). The flux of the GRXE component at the AXP field ($l = 27^\circ.5$, $b = 0^\circ.0$) would be slightly different from that at the GRXE field ($l = 28^\circ.5$, $b = -0^\circ.2$), because the GRXE intensity depends on the galactic latitude (e.g., Yamauchi & Koyama 1993; Kaneda et al. 1997). We assumed that the spatial distribution of the GRXE is modeled by $F(|b|) = F_0 \exp(-|b|/h)$ with a scale height of $h = 0^\circ.5$ and estimated the difference in photon counts in the FoVs of the PIN for both pointings through simulation. As a result, we found that the GRXE flux at the AXP field was about 10% larger than that at the GRXE field. The count rate of 10% of the GRXE + CXB amounts to only 1% of the non-X-ray background of the PIN in the energy range of 12 – 50 keV. Therefore, we neglected the difference of the GRXE count rates between the GRXE and the AXP fields. Consequently, we decided to use the best fitting model at the field ($l = 28^\circ.5$, $b = -0^\circ.2$) as the CXB + GRXE component at the AXP field in subsequent analysis.

(3) Because this observation was performed in the 1/8 window mode of the XISs, a substantial amount of photons from the point source were missing from the FoV. Due to the systematic uncertainty of the PSFs of the XRTs, a systematic discrepancy between the normalization of the XISs and that of the PIN was inevitable. Therefore, we calibrated the cross normalization between the XISs and PIN, using the archival data of the point source, MCG–5–23–16 (data ID: 700002010), which was observed at the HXD nominal pointing and taken in the full window mode of the XISs. We produced the XIS spectra by extracting photons from the region in a manner similar to that described in section 3, setting the distance from the peak position of the point source to a long side of the rectangular FoV of the 1/8 window region to be equal to that for the case of the AXP. We obtained a relative normalization between XIS0 and the PIN of 1.0890, which was used in subsequent analysis.

5.3. Phase-averaged Spectroscopy

We first tried applying a power-law function (PL)⁷, blackbody radiation (BB), and thermal bremsstrahlung (TB) to the AXP component. However, these were found to be statistically unacceptable. Among the pairs (PL + PL, BB + BB, TB + TB, PL + BB, PL + TB, BB + TB), all except the TB + TB showed excesses at a higher energy band or residuals, suggesting it was necessary to add an additional component at the higher energy range.

Among the many possible three-component models we used only the PL + BB and BB +

⁷ We used “pegpwlw” model instead of “powerlaw” model in XSPEC to reduce the off-axis elements of the error matrix used to evaluate the uncertainties of the parameters. In the “pegpwlw” model we set the energy range 1 - 50 keV over which the flux is integrated.

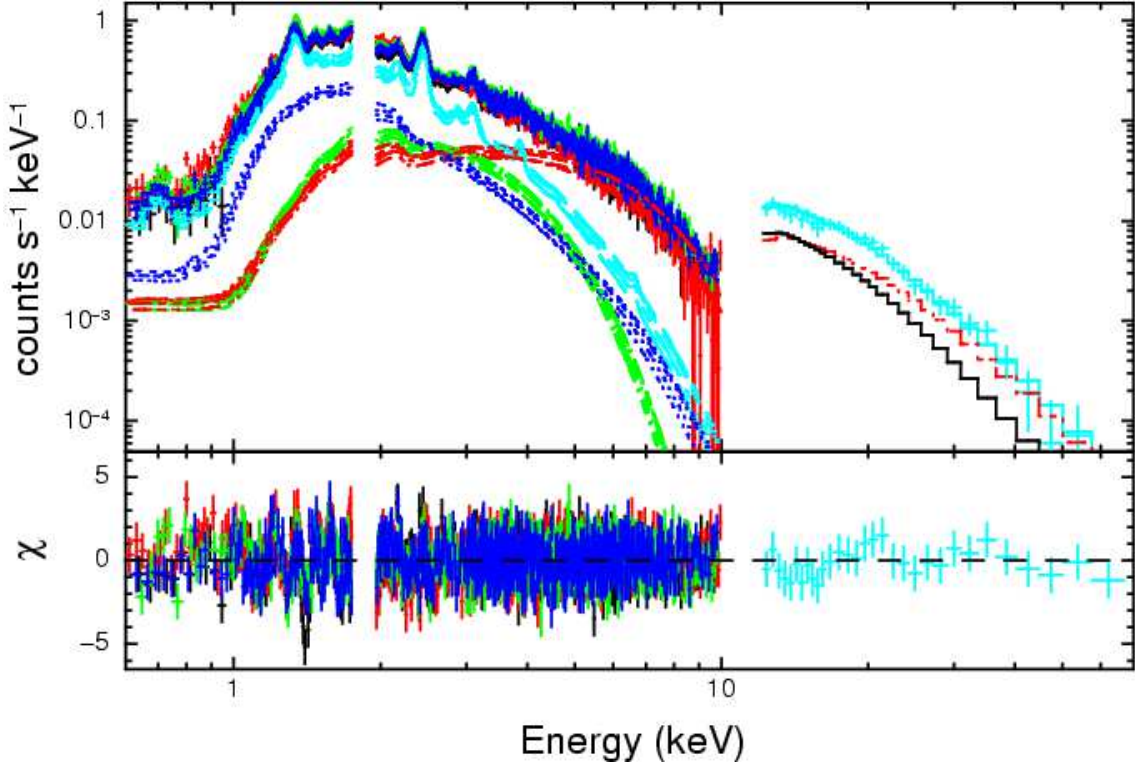


Fig. 3. Phase-averaged spectrum fitted with the BB + PL + PL model after background subtraction (section 3 and subsection 5.2). The data points from XIS0, XIS1, XIS2, XIS3, and PIN are shown as crosses colored black, red, green, blue, and cyan, respectively. The spectral components, the BB, PL in the lower energy range, PL in the higher energy range, SNR, and CXB + GRXE are shown in the histograms colored green, blue, red, cyan, and black, respectively. Vertical error bars represent the 1σ level.

BB models for the lower energy region, because they are familiar models for AXPs below ~ 10 keV. When we applied a PL model to the higher energy region, the PL + BB + PL model was found to produce a good fit (table 1 and figure 3). Although the BB + BB + PL model also produced a reasonable fit, the radius of the BB component with the lower temperature became too large in comparison with the radius of neutron stars (~ 10 km) (table 1).

In the case of the PL + BB + PL model the photon index for the hard X-ray component was $1.62^{+0.05}_{-0.05}(\text{stat})^{+0.16}_{-0.17}(\text{syst})$ (table 1). Since the photon index could mimic that of thermal bremsstrahlung below the exponential cutoff energy⁸, we tried applying a PL + BB + TB model. It resulted in a comparatively good fit (table 1). The BB + BB + TB model was also good, although there was a similar problem in the blackbody radius as in the case of the BB + BB + PL model. The results of the spectral fits are summarized in table 1.

⁸ The slope of a thermal bremsstrahlung spectrum below the exponential cutoff energy exhibits two different dependencies on plasma temperature (kT) in the energy range of the PIN (10 - 50 keV). These are the Gaunt factor and a round-off of the exponential cutoff ($\exp(-E/kT)$). Details of the former dependency were shown in Kellogg, Baldwin & Koch (1975) and the result was included in the “bremss” model in XSPEC.

5.4. Phase-resolved Spectroscopy

We divided the event data into 8 equally wide phase intervals and constructed the phase-resolved spectra by the same procedure shown in subsection 5.2. We rebinned the PI spectra of the XISs so that N_{\min} (see subsection 5.2) was 50, 100 and 50 for the energies below 1.1, between 1.1 and 4.0 and above 4.0 keV, respectively. We used $N_{\min} = 300$ counts for the PIN spectra. We fitted each phase-resolved spectrum by fixing the constant parameters during all phases to the best values obtained by the phase-averaged spectroscopy (sections 5.2 and 5.3). The fixed parameters were the gains, the normalizations of the XISs and PIN, the normalization of the SNR component and the column density for the line of sight (N_H). Figures 4 and 5 show the variations of the parameters when the spectra were fitted with the BB + PL + PL and BB + BB + PL models, respectively. For the latter model the photon indices of the power-law components were constant during all phases within a 90% confidence level (C.L.). Then, we fixed those indices with the best value obtained by the phase-averaged spectroscopy (table 1). In these figures the vertical bars represent a statistical error of 1σ , not including the errors caused by the systematic uncertainty of the non-X-ray background.

5.5. Spectroscopy of the Pulsed Component

The spectrum of the pulsed component was produced by subtracting the off-pulse spectrum in the phase range 0.0 – 0.1 from the spectrum with a range between 0.1 and 1 using `mathpha`. We constructed a XIS-FI spectrum by adding the spectra of XIS0, XIS2 and XIS3, and also a response by using `marfrmf` and `addrmf`. We rebinned the PI spectra of XIS-FI, XIS-BI and PIN so that N_{\min} (see subsection 5.2) was 500, 500 and 400, respectively. We fitted the spectrum of the pulsed component with PL and BB + PL models by fixing the N_H to the best value obtained from fitting the phase-averaged spectrum using the BB + PL + PL model (subsection 5.3 and table 1). Here, we averaged the gain parameters of XIS0, XIS2 and XIS3 to obtain that of XIS-FI, and also renormalized and fixed the parameters $c_{\text{XIS-BI}}$ and c_{PIN} . The fitting results are shown in table 2. When the spectrum was fitted with the PL model, there appeared to be a global concave residual, although the statistics of the fit was still acceptable. When it was fitted with the PL + BB model, this residual disappeared and the χ^2 value improved significantly with a F-test statistics of 9.80 (a probability of 1.7×10^{-4}). Figure 6 shows the spectrum of the pulsed component fitted with the PL + BB model.

5.6. Phase-resolved Spectroscopy of the Pulsed Component

We divided the data into the following phase intervals: off-pulse (0.0 – 0.1), rising wing of the first pulse (0.1 – 0.3), top of the first pulse (0.3 – 0.5), valley (0.5 – 0.65), top of the second pulse (0.65 – 0.85) and trailing wing of the second pulse (0.85 – 1.0). Phase-resolved spectra of the pulsed component were constructed by subtracting the off-pulse spectrum for intervals other than the off-pulse interval. We produced XIS-FI spectra by the procedure

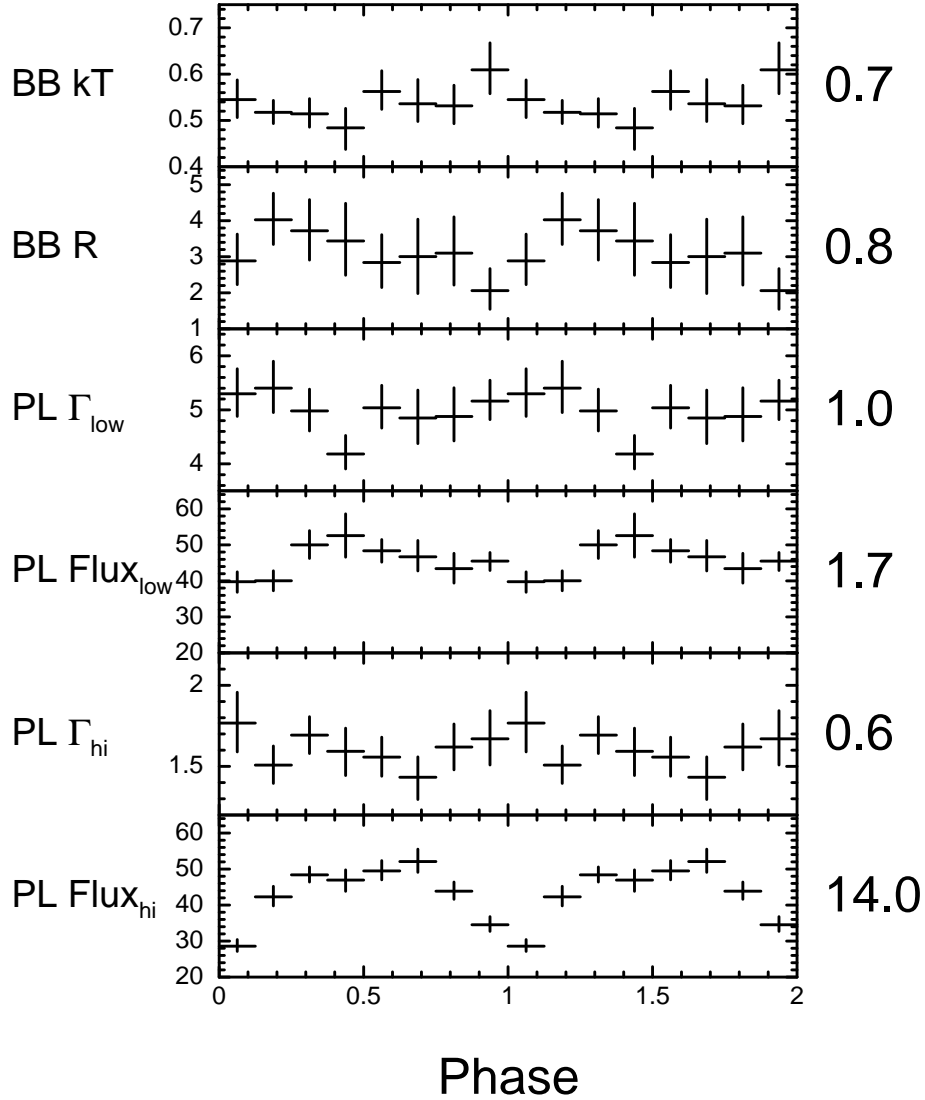


Fig. 4. Variation of the spectral parameters along pulse phases, when the spectra were fitted with a BB + PL + PL model. The panels from the top to the bottom show the temperature of the BB component, the radius of the BB emission region on the neutron star surface, the photon index of the PL component in the lower energy range, the unabsorbed flux of the PL component in the lower energy range, the photon index of the PL component in the higher energy range and the unabsorbed flux of the PL component in the higher energy range. The fluxes are in an energy range of 1.0 – 50.0 keV. The temperatures, radii and fluxes are shown in units of keV, km and $\times 10^{-12}$ erg s $^{-1}$ cm $^{-2}$, respectively. Vertical error bars represent a 1σ level. At the right of each panel the reduced χ^2 is shown for the case where the profile was fitted with a constant model and the degree of freedom was 7.

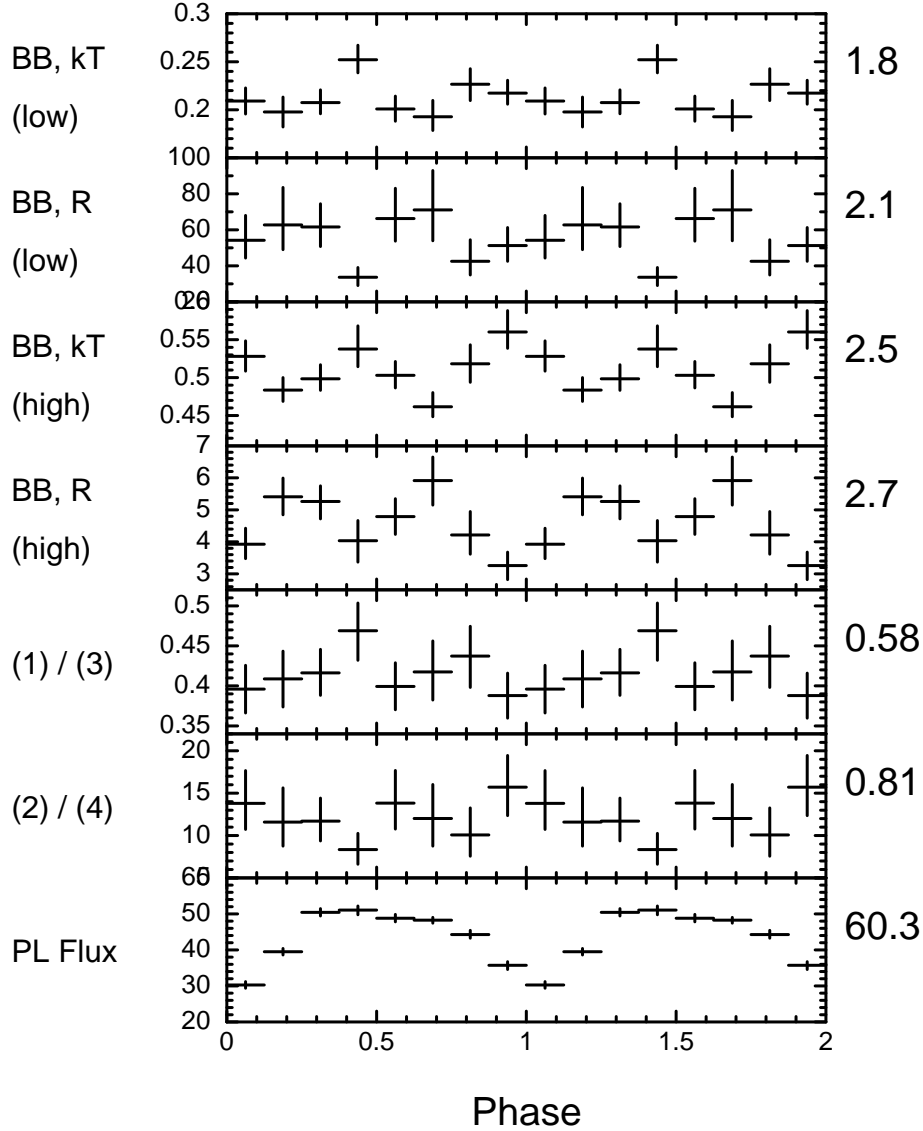


Fig. 5. Variation of spectral parameters along pulse phases, when the spectra were fitted with a BB + BB + PL model. Here, the photon indices of the power-law components were fixed with the best value obtained from the phase-averaged spectroscopy (table 1). The top two panels show the temperature and radius of the emission region on the neutron star surface of the BB component in the lower energy range. The third and fourth panels show those in the higher energy range. The fifth and sixth panels show the ratios of the first to the third panel and the second to the fourth, respectively. The bottom panel shows the unabsorbed flux of the PL component in an energy range of 1.0 – 50.0 keV. The temperatures, radii and fluxes are shown in units of keV, km and $\times 10^{-12}$ erg s $^{-1}$ cm $^{-2}$, respectively. Vertical error bars represent a 1σ level. At the right of each panel the reduced χ^2 is shown for the case where the profile was fitted with a constant model and the degree of freedom was 7.

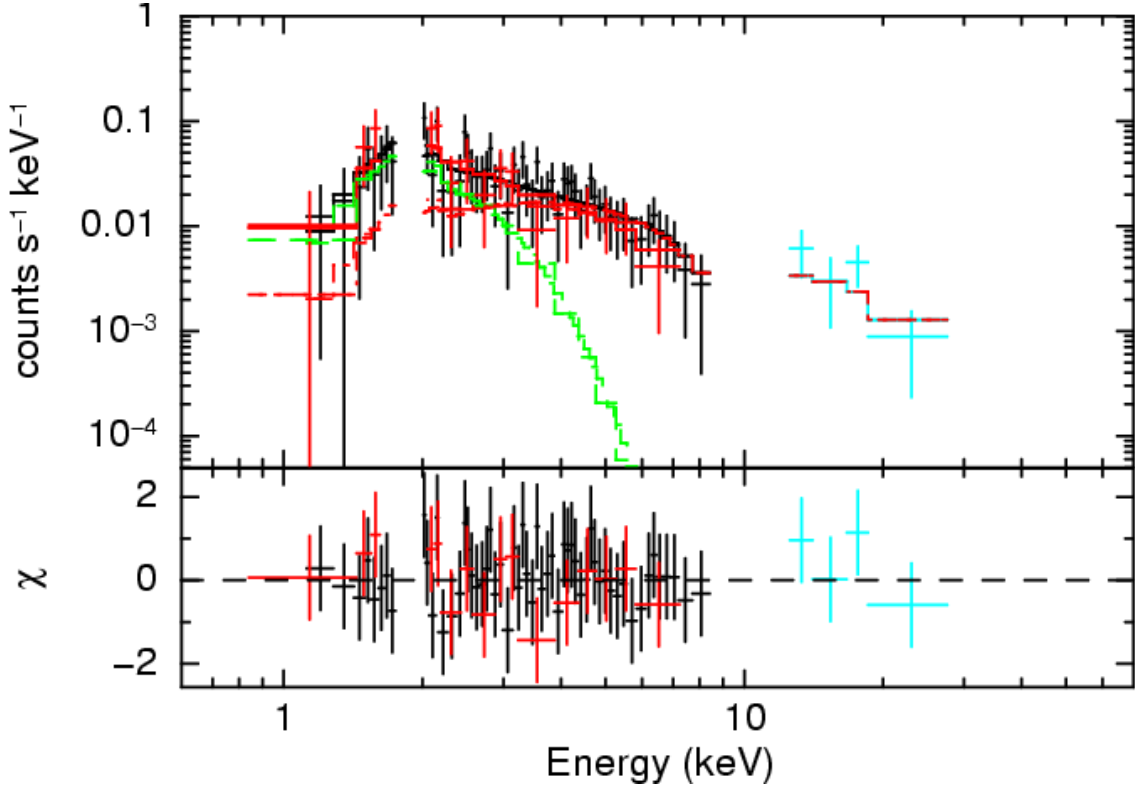


Fig. 6. Spectrum of the pulsed component fitted with a PL + BB model. The data points from the XIS-FI, XIS-BI and PIN are shown as crosses colored black, red and cyan, respectively. The BB and PL spectral components are shown as green and red histograms, respectively. Vertical error bars represent a 1σ level.

described in subsection 5.5. We rebinned the PI spectra of XIS-FI, XIS-BI and PIN so that N_{\min} (see subsection 5.2) was 100, 100 and 50, respectively. We first fitted all the phases with BB + PL models by fixing the N_H to the best value obtained by fitting the phase-averaged spectrum using the BB + PL + PL model (subsection 5.3 and table 1) and allowing the other parameters to vary. In this case fits for all phases were acceptable within the 90% C.L. and the parameters showed no significant deviation from the mean values. We then fixed the blackbody temperature to the best value obtained by fitting the pulsed component spectrum using the BB + PL model (subsection 5.5 and table 2). In this case all of the fits were also acceptable within the 90% C.L. The variations of the parameters are shown in figure 7.

5.7. Comparison of the Suzaku spectral results with other high-energy instruments

Finally, we made νF_ν plots for the total (phase-averaged spectrum) and pulsed components (figures 8 and 9, respectively). Here, the phase-averaged and pulsed component Suzaku spectra are unfolded by the BB + PL + PL and the BB + PL models with the best fitting parameters of tables 1 and 2, respectively. In figure 8 the flux of around 20 – 50 keV for the Suzaku data is marginally consistent with that of INTEGRAL IBIS ISGRI. The photon index

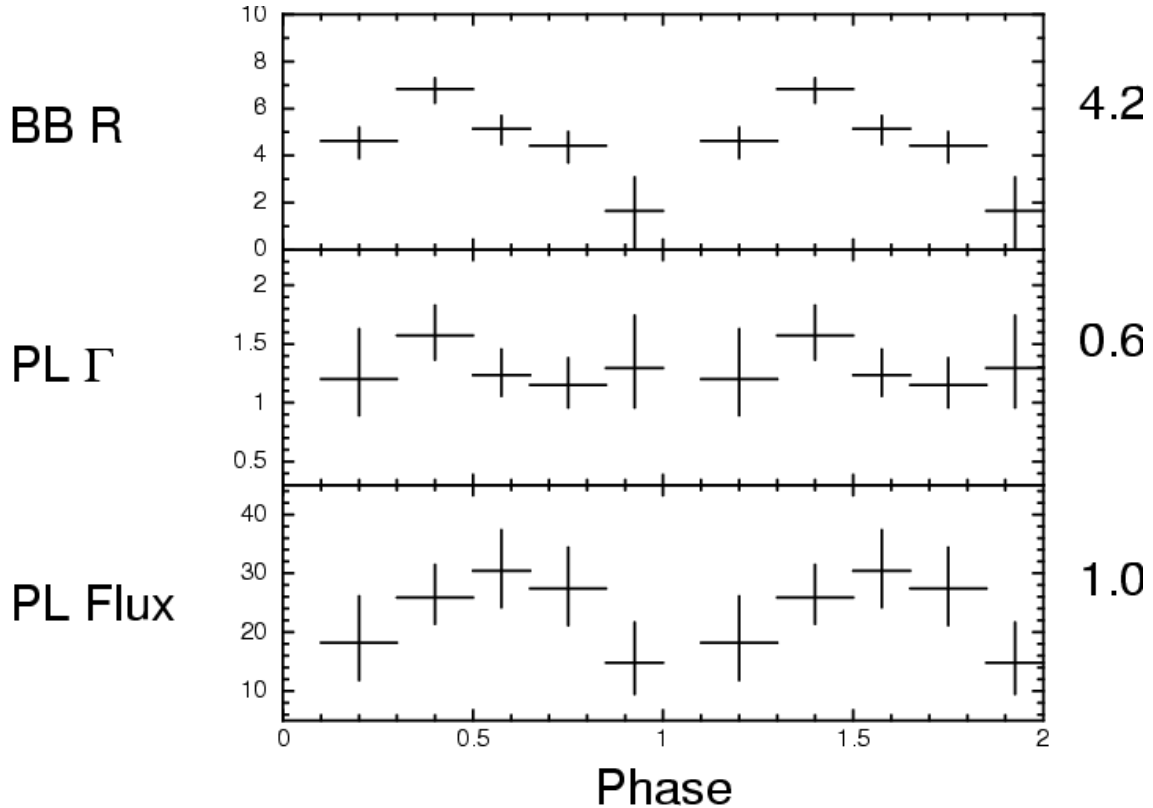


Fig. 7. Variation of spectral parameters along pulse phase, when the pulsed spectra were fitted with a BB + PL model with the temperature fixed to the best fitting value (see text). The panels from the top to the bottom show the radius of the BB emission region on the neutron star surface, the photon index of the PL component and the unabsorbed flux of the PL component. The fluxes are in an energy range of 1.0 – 50.0 keV. The radii and fluxes are shown in units of km and $\times 10^{-12}$ erg s $^{-1}$ cm $^{-2}$, respectively. Vertical error bars represent a 1σ level. Horizontal bars show the phase binning described in section 5.6. At the right of each panel the reduced χ^2 value is shown for the case where the profile was fitted with a constant model and the degree of freedom was 4.

of the PL component in the higher energy range ($1.62^{+0.05}_{-0.05}(\text{stat})^{+0.16}_{-0.17}(\text{syst})$) is also marginally consistent with that of INTEGRAL (1.32 ± 0.11), where the difference corresponds to 1.5σ if both statistical and systematic errors are assumed to be 1σ and combined as a root-mean-squared value. In figure 9 the pulsed component flux of the XISs is consistent with that of RXTE PCA in the 2.5–8 keV range. However, the flux bin of the PIN in the 12–20 keV range is marginally larger than that of RXTE PCA by a factor of 2.8 and with a significance of 1.9σ level.

6. Discussion

In the previous Chandra observations (Morii et al. 2003) the spectrum of the AXP 1E 1841–045 was described well in the energy range 0.6 – 7.0 keV by a combination of a blackbody (BB) and a power-law (PL) function or that of two blackbodies. In the BB + PL model the

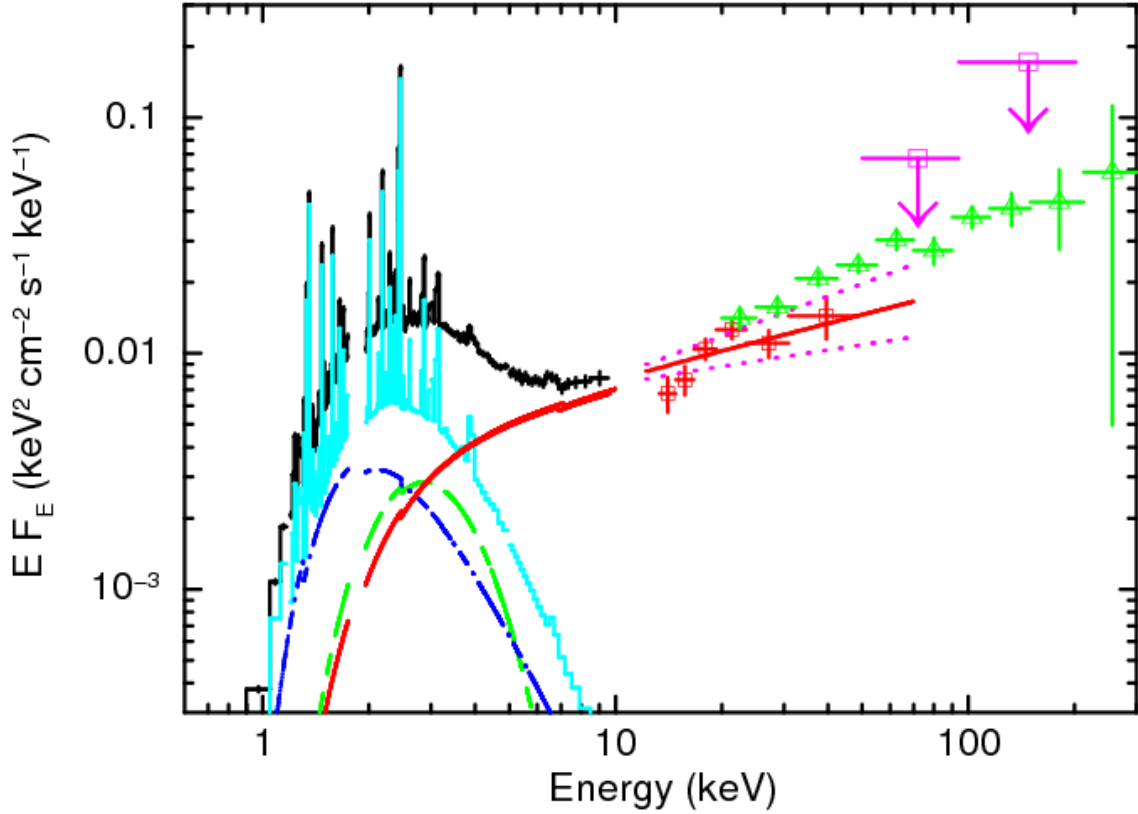


Fig. 8. A νF_ν plot for phase-averaged total (pulsed + DC) spectrum with interstellar absorption obtained by the Suzaku observation compared with that of INTEGRAL IBIS ISGRI (Kuiper, den Hartog, & Hermsen 2008). The vertical and horizontal axes are energy-scaled flux EF_E and energy in units of $\text{keV}^2 \text{cm}^{-2} \text{s}^{-1} \text{keV}^{-1}$ and keV, respectively. The phase-averaged spectrum of Suzaku is produced by unfolding in the BB + PL + PL with the best fitting parameters of table 1. The phase-averaged fluxes of XIS-FI and PIN are shown as black crosses and red crosses with square symbols, respectively. The upper limits of GSO are shown as magenta downward arrows corresponding to the 2% uncertainty of the non-X-ray background. The blackbody, power-laws at lower and higher energy and supernova remnant components of Suzaku are shown as green dashed, blue dot-dashed, red solid and cyan solid lines, respectively. The range of the systematic uncertainty in the PIN for the high energy power-law component is shown as two magenta dotted lines. All vertical error bars represent a 1σ level. For comparison the INTEGRAL ISGRI 20–300 keV spectrum (Kuiper, den Hartog, & Hermsen 2008) is also plotted as green crosses with triangle symbols.

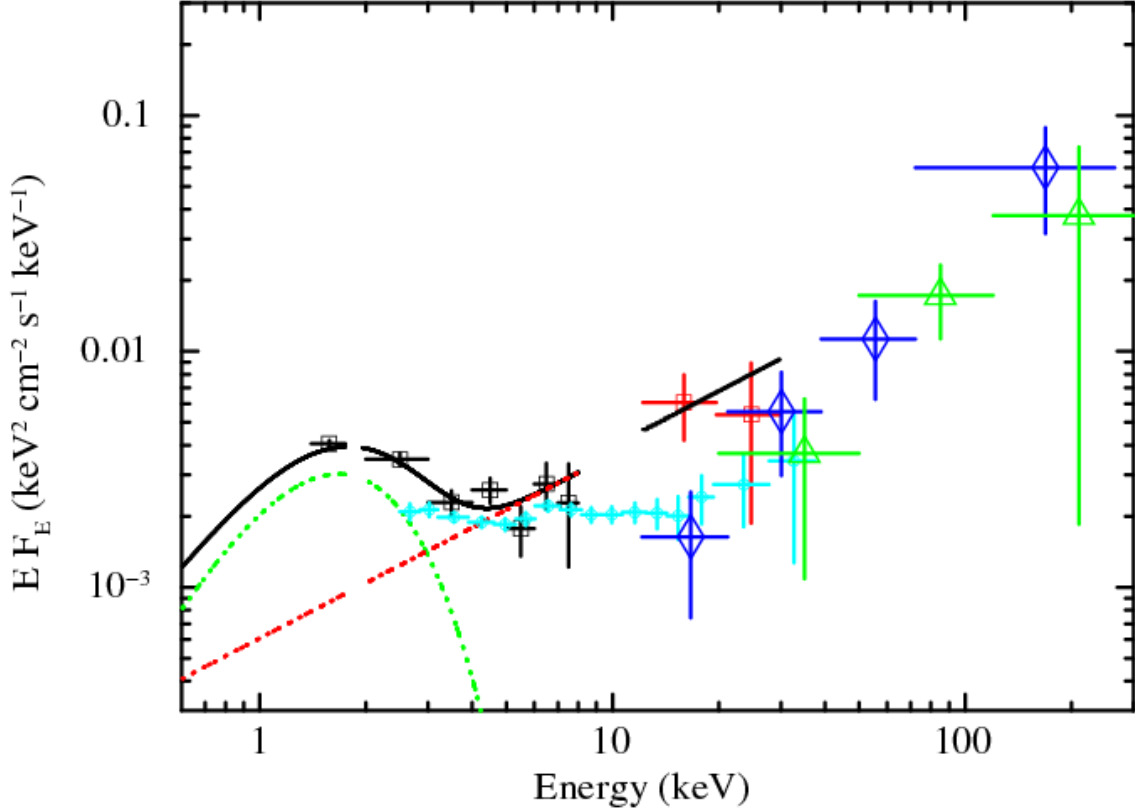


Fig. 9. An unabsorbed νF_ν plot for the pulsed component obtained from the Suzaku observation compared with those of RXTE PCA, RXTE HEXTE and INTEGRAL IBIS ISGRI (Kuiper et al. 2006; Kuiper, den Hartog, & Hermsen 2008). The vertical and horizontal axes are energy-scaled flux EF_E and energy in units of $\text{keV}^2 \text{cm}^{-2} \text{s}^{-1} \text{keV}^{-1}$ and keV, respectively. The pulsed component spectrum of Suzaku is produced by unfolding in the BB + PL models with the best fitting parameters of table 2. The total model, blackbody and power-law components are shown as black solid, green and red dotted lines, respectively. The XIS-FI and PIN data are shown as black and red crosses with square symbols. All vertical error bars represent a 1σ level. For comparison RXTE PCA, RXTE HEXTE and INTEGRAL IBIS ISGRI (Kuiper et al. 2006; Kuiper, den Hartog, & Hermsen 2008) are shown as crosses with cyan small circle, blue diamond and green triangle symbols, respectively.

temperature and photon index were determined to be $kT_{\text{BB}} = 0.44 \pm 0.02$ keV and $\Gamma = 2.0 \pm 0.3$. Since the photon index was the flattest among AXPs and close to those of SGRs (~ 2), Morii et al. (2003) concluded that this AXP was the closest object to SGRs among AXPs. Nonetheless, owing to the hard X-ray component above ~ 20 keV discovered by Kuiper, Hermsen, & Mendez (2004) these conclusions had to be modified, because a substantial amount of the hard X-ray component is thought to be included in the Chandra spectrum. This expectation has been confirmed by our Suzaku observation and an additional component in the hard X-ray band turns out to be necessary.

When the spectrum was modeled with a BB + PL + PL model, it produced the best fit among the models we applied (table 1). This modeling was the most plausible because the hard X-ray spectrum was well modeled by a power-law function above ~ 20 keV in the result of Kuiper, Hermsen, & Mendez (2004). On the other hand, we found that the photon index of the lower energy range $\Gamma_{\text{low}} = 4.99^{+0.29}_{-0.29}(\text{stat})^{+0.28}_{-0.30}(\text{syst})$ is quite different from that of the previous Chandra result (section 1 and at the beginning of this section). This discrepancy was caused by the different energy coverage of the spectroscopic data between Suzaku and other satellites. While the spectra obtained by the other satellites could be fitted by only one or two continuum components, we could fit this AXP spectrum satisfactorily only by three continuum component due to the much wider energy coverage of our Suzaku measurements. Therefore, Suzaku observations of AXPs and SGRs are important for determination of spectra of magnetars. In particular, the relationship between spectral properties and spin-down rates among AXPs and SGRs obtained by Marsden & White (2001) must be reexamined by Suzaku observations. Ironically, as shown in figure 3 the PL component with the steep index does not contribute to the hard tail shape but rather the excess component in the lower energy range. Therefore, the physical meaning of this PL component should be reconsidered.

The photon index of the hard X-ray component in the BB + PL + PL model was similar to that of thermal bremsstrahlung below the exponential cutoff energy (see subsection 5.3). Thus, a PL + BB + TB model could also fit the spectrum (table 1). The temperature of the thermal bremsstrahlung was $kT_{\text{TB}} = 51.7^{+14.1}_{-8.8}(\text{stat})^{+68.0}_{-22.1}(\text{syst})$ keV, implying the existence of a high energy cut-off above the energy range of the PIN. Nonetheless the INTEGRAL ISGRI data, collected over many years (figure 8) contradict this model, because the data shows that the cut-off energy is above about 200 – 300 keV. However, there still remain a possibility that the temperature of the thermal bremsstrahlung was low during the Suzaku observation due to short time scale variability.

In the pulsed component spectrum of figure 9 the flux of the XISs is consistent with that of RXTE PCA. Nonetheless, that of the PIN for 12 – 20 keV is marginally higher than that of RXTE PCA and HEXTE. This discrepancy could be another indication for the spectral variability of the hard tail component over a short time scale. Further Suzaku observation of this source will be needed to confirm this kind of variability in the hard tail.

We showed for the first time analysis of phase-resolved spectra for the total (including the DC component) and the pulsed component (excluding the DC component) in subsection 5.5 and 5.6, respectively. The shift of the peak phases for the blackbody radii and the PL fluxes in the pulsed component spectra (figure 7) is consistent with the peak shifts of pulse profiles in figure 1. This shift indicates the existence of two emission regions: one is a hot spot on the neutron star surface with blackbody emission and the other is of non-thermal origin rather than two hot spots on the surface. The latter possibility was first put forward by Morii et al. (2003) and turns out to be unlikely on the basis of this study. This interpretation is also confirmed by the peak shift of the two PL fluxes in figure 4 (the forth and the bottom panels). Here, the PL component in the lower energy range substantively represents the soft excess component as discussed above.

The photon index of the pulsed component (table 2) is similar to those of several young and middle-aged rotation powered pulsars such as Vela pulsar, PSR B1509–58 and PSR J1846–0258 (see Kuiper et al. 2006, Kuiper & Hermsen 2009 and references therein). Then, the outer-gap or slot-gap models describing the production of gamma-ray emission of rotation-powered pulsars are promising to explain the hard X-ray emission of magnetars.

When the phase-averaged total spectrum was fitted with the BB + BB + PL model, the area of the emission region of the blackbody component with the lower temperature was too large in comparison with the surface area of neutron stars (table 1). Therefore, these models are physically unacceptable at first glance. Nonetheless, Nakagawa et al. (2009) showed interesting relationships among the parameters of the BB + BB model in the spectra of magnetars below about 10 keV, which may offer clues to the underlying physics of magnetars. For example, Özel (2001) showed that the shape of the spectra of magnetars is deformed by cyclotron resonant scattering in the magnetosphere and the resulting spectra are well fitted by BB + BB and BB + PL models. We then checked whether the phase-resolved spectra of 1E 1841–045 also follow this relationship. In what follows, we will treat the BB + BB model simply as an empirical model to represent the spectrum approximately.

When the spectra of each pulse phase interval was fitted with the BB + BB + PL model, we found a significant anti-correlation between the temperatures and radii of the two blackbody components (figure 5). This anti-correlation is clearly seen in figure 10. It is similar to the anti-correlation reported by Nakagawa et al. (2009) among phase-averaged spectra of various AXPs and SGRs. Nakagawa et al. (2009) showed that the blackbody radii (R) and temperatures (kT) follow $R \propto (kT)^{-2}$, meaning that the bolometric luminosities of the blackbody components are constant. As indicated by the two dashed lines in figure 10, the R and kT of the two blackbody components with the lower and higher temperature can be fitted to a $R \propto (kT)^{-2}$ function at a 90% C.L. This is the first time such a relationship has been found in the phase-resolved spectra of AXPs and SGRs.

We also tested other correlations between temperatures (kT) and radii (R) of the two

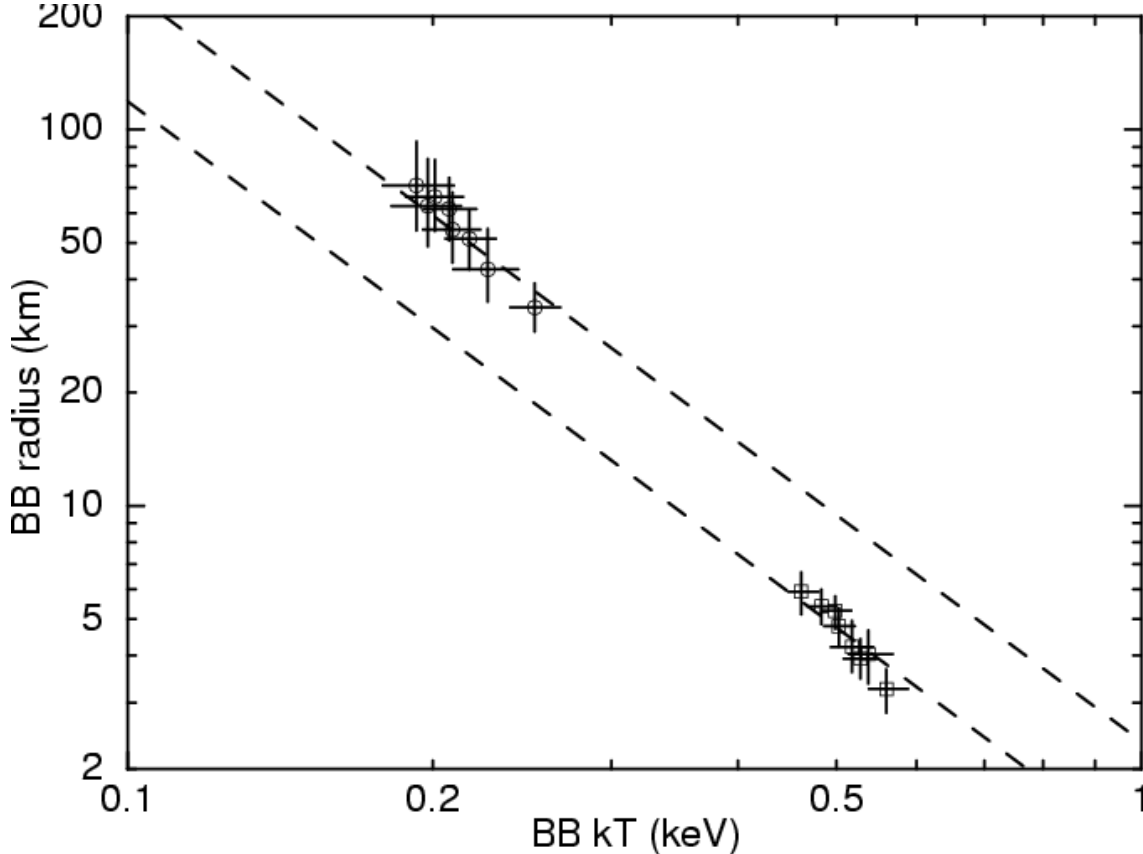


Fig. 10. Anti-correlation between radii (R) and temperatures (kT) for the blackbody components with lower and higher temperatures, when the phase-resolved spectra were fitted with a BB + BB + PL model. The crosses with circular symbols and those with square symbols denote lower and higher temperatures, respectively. Error bars represent 1σ levels. The dashed lines represent a constant blackbody bolometric luminosity, that is $R \propto (kT)^{-2}$.

blackbodies reported by Nakagawa et al. (2009). These are $kT_{\text{LT}}/kT_{\text{HT}} \sim 0.4$ and $R_{\text{LT}}/R_{\text{HT}} \sim 10$, where the subscripts LT and HT denote the lower and higher temperatures, respectively. We found that these correlations also hold for the phase-resolved spectra of the AXP (the fifth and sixth panels of figure 5 and figure 11) for the first time in phase-resolved spectra of AXPs and SGRs. In figure 11 the ratios are calculated to be $kT_{\text{LT}}/kT_{\text{HT}} = 0.41 \pm 0.01$ and $R_{\text{LT}}/R_{\text{HT}} = 10.7 \pm 0.8$ by fitting the points with a proportional expression. In addition, we tested these correlations by calculating the Spearman rank-order correlation coefficients (r_s ; Press et al. 1992) for eight points with asymmetrical errors. Here, the errors are taken into account by a Monte Carlo method with a two dimensional Gaussian probability function with asymmetrical sigmas. The results were $0.48^{+0.38}_{-0.51}$ and $0.43^{+0.41}_{-0.55}$ (90% C.L.) respectively, suggesting these values are moderately correlated. These correlations suggest that the spectral shape exhibited by blackbodies with two different temperatures with such constraints can approximate the intrinsic spectral shape of magnetars. This spectral shape is actually a self-similar function

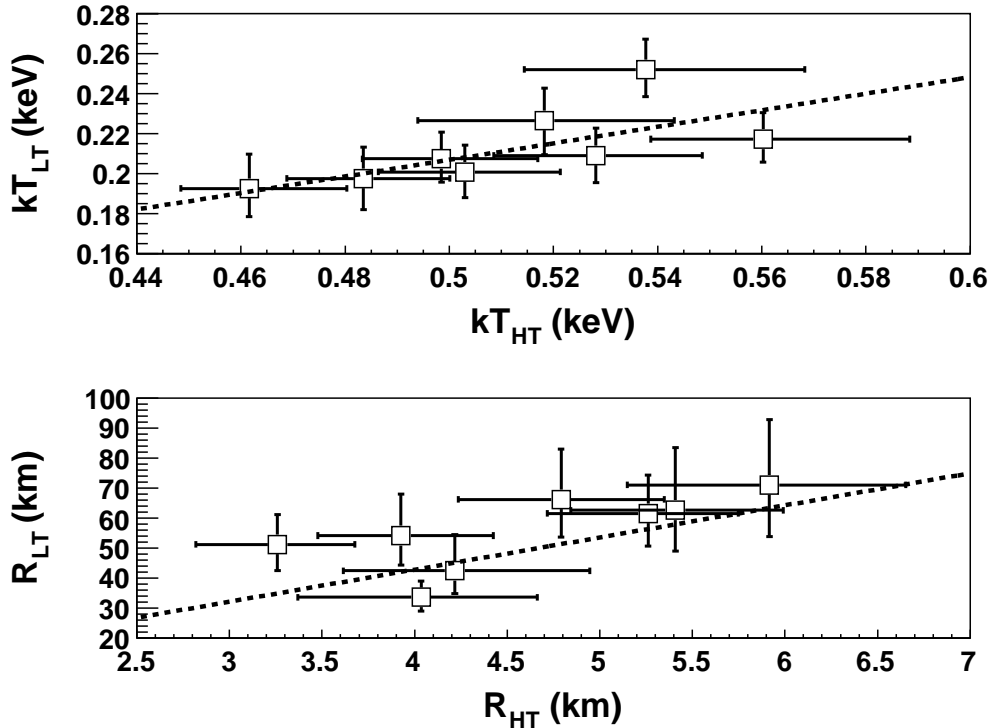


Fig. 11. Correlation between temperatures (kT) and radii (R) for blackbody components with lower (LT) and higher (HT) temperatures, when the phase-resolved spectra were fitted with a BB + BB + PL model. Error bars represent 1σ levels. The dotted lines shows $kT_{LT} = 0.41kT_{HT}$ and $R_{LT} = 10.7R_{HT}$.

with two free parameters.

In summary, our Suzaku observation and analysis of the AXP 1E 1841–045 showed that a BB + PL + PL model can best represent the phase-averaged spectrum over a wide energy range, simultaneously. Detailed phase-resolved spectroscopy was also carried out and the existence of two emission regions was indicated, a hot spot with blackbody emission and another region with non-thermal emission. The BB + BB + PL model was also statistically acceptable, although physically unacceptable. Nonetheless, we found correlations between the radii and temperatures of the two blackbodies in the phase-resolved spectra for the first time in phase-resolved spectra of AXPs and SGRs. These correlations may provide important insights into the underlying emission mechanisms of magnetars.

We express our gratitude to L. Kuiper for suggesting detailed revisions to this manuscript. We are grateful to all the members of the Suzaku Science Working Group and Suzaku Help. We appreciate Dai Takei at Rikkyo University for the Suzaku analysis. Mikio Morii acknowledges support by a Grant-in-Aid for Young Scientists (B)(21740140) and the Global COE Program, “Nanoscience and Quantum Physics Project of the Tokyo Institute of Technology.”

References

- Beloborodov, A. M. & Thompson, C. 2007, *ApJ*, 657, 967
- Borkowski, K. J., Lyerly, W. J. & Reynolds, S. P. 2001, *ApJ*, 548, 820
- Buccheri, R. *et al.* 1983, *A&A*, 128, 245
- Camilo, F. Ransom, S. M., Halpern, J. P., Reynolds, J., Helfand, D. J., Zimmerman, N. & Sarkissian, J. 2006, *Nature*, 442, 892
- Camilo, F., Ransom, S. M., Halpern, J. P. & Reynolds, J. 2007, *ApJ*, 666, L93
- den Hartog, P. R., Kuiper, L., Hermsen, W., Kaspi, V. M., Dib, R., Knodlseder, J. & Gavriil, F. P. 2008, *A&A*, 489, 245
- den Hartog, P. R., Kuiper, L. & Hermsen, W. 2008, *A&A*, 489, 263
- Dib, R., Kaspi, V. M. & Gavriil, F. P. 2008, *ApJ*, 673, 1044
- Hellier, C. 1994, *MNRAS*, 271, L21
- Heyl, J. S. & Hernquist, L. 2005, *MNRAS*, 362, 777
- Kaneda, H., Makishima, K., Yamauchi, S., Koyama, K., Matsuzaki, K. & Yamasaki, N. Y. 1997, *ApJ*, 491, 638
- Kellogg, E., Baldwin, J. R. & Koch, D. 1975, *ApJ*, 199, 299
- Kokubun, M. *et al.* 2007, *PASJ*, 59, S53
- Koyama, K. *et al.* 2007, *PASJ*, 59, S23
- Kriss, G. A., Becker, R. H., Helfand, D. J. & Canizares, C. R. 1985, *ApJ*, 288, 703
- Kuiper, L., Hermsen, W. & Mendez, M. 2004, *ApJ*, 613, 1173
- Kuiper, L., Hermsen, W., den Hartog, P. R. & Collmar, W. 2006, *ApJ*, 645, 556
- Kuiper, L., den Hartog, P. R. & Hermsen, W. 2008, *Conference Proc. "3rd International Maxi Workshop,"* 10-12 June, 2008, Wako, Saitama, Japan (arXiv:0810.4801)
- Kuiper, L. & Hermsen, W. 2009, *A&A*, 501, 1031
- Marsden, D. & White, N. E. 2001, *ApJ*, 551, L155
- Mereghetti, S. & Stella, L. 1995, *ApJ*, 442, L17
- Mitsuda, K. *et al.* 2007, *PASJ*, 59, S1
- Morii, M., Sato, R., Kataoka, J. & Kawai, N. 2003, *PASJ*, 55, L45
- Nakagawa, Y. E., Yoshida, A., Yamaoka, K. & Shibazaki, N. 2009, *PASJ*, 61, 109
- Özel, F. 2001, *ApJ*, 563, 276
- Press, W. H. *et al.* 1992, "Numerical Recipes in C, Second Edition," Cambridge University Press
- Sanbonmatsu, K. Y. & Helfand, D. J. 1992, *AJ*, 104, 2189
- Serlemitsos, P. J. 2007, *PASJ*, 59, S9
- Takahashi, T. *et al.* 2007, *PASJ*, 59, S35
- Terada *et al.* 2008, *PASJ*, 60, S25
- Thompson, C. & Beloborodov, A. M. 2005, *ApJ*, 634, 565
- Tian, W. W. & Leahy, D. A. 2007, *ApJ*, 677, 292
- van Paradijs, J., Taam, R. E. & van den Heuvel, E. P. J. 1995, *A&A*, 299, L41
- Vasisht, G. & Gotthelf, E. V. 1997, *ApJ*, 486, L129
- Woods, P. M. & Thompson, C., "Soft Gamma repeaters and anomalous X-ray pulsars: magnetar candidates," in *Compact Stellar X-ray Sources*, edited by Lewin, W. H. G. and van der Klis, M.,

Cambridge University Press, New York, 2006, pp. 547–586 (astro-ph/0406133).
Yamauchi, S. & Koyama, K. 1993, ApJ, 404, 620

Table 1. Fits to the phase-averaged total spectrum of 1E 1841–045

BB + PL + PL		
parameter	units	value \pm stat [†] \pm syst [‡]
N_{H}	10^{22} cm^{-2}	$2.866^{+0.020+0.008}_{-0.020-0.010}$
kT_{BB}	keV	$0.536^{+0.015+0.027}_{-0.014-0.026}$
R_{BB}	km @ 8.5 kpc	$3.16^{+0.35+0.46}_{-0.34-0.45}$
Γ_{low}		$4.99^{+0.29+0.28}_{-0.29-0.30}$
Flux _{low} *	$10^{-12} \text{ erg/cm}^2/\text{s}$ @ 1 – 50 keV	$46.5^{+2.4+1.1}_{-2.3-1.1}$
Γ_{high}		$1.62^{+0.05+0.16}_{-0.05-0.17}$
Flux _{high} *	$10^{-12} \text{ erg/cm}^2/\text{s}$ @ 1 – 50 keV	$43.7^{+0.9+3.0}_{-0.9-2.0}$
$\chi^2/\text{d.o.f.} = 2530 / 2154 = 1.175$		
BB + PL + TB		
N_{H}	10^{22} cm^{-2}	$2.851^{+0.019+0.009}_{-0.018-0.008}$
kT_{BB}	keV	$0.569^{+0.014+0.015}_{-0.014-0.019}$
R_{BB}	km @ 8.5 kpc	$2.60^{+0.29+0.39}_{-0.28-0.28}$
Γ		$4.56^{+0.26+0.24}_{-0.25-0.19}$
Flux *	$10^{-12} \text{ erg/cm}^2/\text{s}$ @ 1 – 50 keV	$48.2^{+1.9+0.6}_{-1.8-0.6}$
kT_{TB}	keV	$51.7^{+14.1+68.0}_{-8.8-22.1}$
$\text{EM}_{\text{TB}} (= n^2V)$	10^{57} cm^{-3} @ 8.5 kpc	$7.47^{+0.19+0.73}_{-0.22-0.02}$
$\chi^2/\text{d.o.f.} = 2534 / 2154 = 1.176$		
BB + BB + PL		
N_{H}	10^{22} cm^{-2}	$2.811^{+0.013+0.007}_{-0.009-0.007}$
kT_{BB_1}	keV	$0.211^{+0.009+0.010}_{-0.009-0.010}$
R_{BB_1}	km @ 8.5 kpc	$55.7^{+10.7+9.4}_{-8.3-7.5}$
kT_{BB_2}	keV	$0.505^{+0.008+0.023}_{-0.011-0.022}$
R_{BB_2}	km @ 8.5 kpc	$4.72^{+0.30+0.47}_{-0.27-0.44}$
Γ		$1.70^{+0.04+0.14}_{-0.03-0.14}$
Flux *	$10^{-12} \text{ erg/cm}^2/\text{s}$ @ 1 – 50 keV	$44.3^{+0.8+2.9}_{-0.7-1.8}$
$\chi^2/\text{d.o.f.} = 2541 / 2154 = 1.180$		
BB + BB + TB		
N_{H}	10^{22} cm^{-2}	$2.799^{+0.015+0.005}_{-0.014-0.004}$
kT_{BB_1}	keV	$0.228^{+0.009+0.007}_{-0.009-0.009}$
R_{BB_1}	km @ 8.5 kpc	$44.1^{+6.9+5.8}_{-5.2-3.6}$
kT_{BB_2}	keV	$0.543^{+0.011+0.016}_{-0.010-0.021}$
R_{BB_2}	km @ 8.5 kpc	$4.08^{+0.24+0.43}_{-0.22-0.29}$
kT_{TB}	keV	$36.0^{+4.7+26.0}_{-4.0-12.6}$
$\text{EM}_{\text{TB}} (= n^2V)$	10^{57} cm^{-3} @ 8.5 kpc	$8.03^{+0.09+0.27}_{-0.09-0.01}$

Table 1. (Continued.)

$$\chi^2/\text{d.o.f.} = 2557 / 2154 = 1.187$$

† Statistical error of 1σ .

‡ Systematic error due to the 3% uncertainty in the non-X-ray background of the PIN⁶.

* Unabsorbed flux.

Table 2. Fits to the spectrum of the pulsed component of 1E 1841–045

PL †		
parameter	units	value \pm stat(1σ)
Γ		$2.45^{+0.20}_{-0.21}$
Flux *	10^{-12} erg/cm ² /s @ 1 – 50 keV	$13.7^{+1.1}_{-0.9}$
$\chi^2/\text{d.o.f.} = 47.1 / 75 = 0.627$		
BB + PL †		
kT_{BB}	keV	$0.37^{+0.06}_{-0.05}$
R_{BB}	km @ 8.5 kpc	$5.3^{+2.7}_{-1.7}$
Γ		$1.35^{+0.30}_{-0.25}$
Flux *	10^{-12} erg/cm ² /s @ 1 – 50 keV	$21.8^{+6.2}_{-5.1}$
$\chi^2/\text{d.o.f.} = 37.1 / 73 = 0.508$		

† N_{H} is fixed to the best value obtained by the phase-averaged spectral analysis of the total emission using the BB + PL + PL model (see subsection 5.3 and table 1).

* Unabsorbed flux.